

## Water Splitting

## Syntheses of Exceptionally Stable Aluminum(III) Metal–Organic Frameworks: How to Grow High-Quality, Large, Single Crystals

Yuanyuan Guo<sup>+, [a]</sup> Jun Zhang<sup>+, [b]</sup> Long-Zhang Dong,<sup>[a]</sup> Yan Xu,<sup>[c]</sup> Wei Han,<sup>[a]</sup> Min Fang,<sup>\*, [a, d]</sup> Hong-Ke Liu,<sup>[a, d]</sup> Yong Wu,<sup>\*, [a]</sup> and Ya-Qian Lan<sup>\*, [a]</sup>

**Abstract:** The difficulty of obtaining large single crystals of aluminum carboxylate metal–organic frameworks (MOFs) for structure determinations has limited the development of these water and thermally stable MOFs. Herein, how large single crystals of known MIL-53(Al) and the first two tetrahedral ligand-based, visible-light-absorbing 3D Al-MOFs, [Al<sub>3</sub>(OH)<sub>3</sub>(HTCS)<sub>2</sub>] (AITCS-1) and [Al<sub>5</sub>O<sub>2</sub>(OH)<sub>3</sub>(TCS)<sub>2</sub>(H<sub>2</sub>O)<sub>2</sub>] (AITCS-2; TCS = tetrakis(4-oxycarbonylphenyl)silane), are obtained in the presence of hydrofluoric or formic acid for conventional single-crystal diffraction measurements is presented. The technique of obtaining those single crystals has potential to be a general method for obtaining large and good-quality single crystals of Al-MOFs. AITCS-1 and -2 are

stable over a wide pH range (1–11), and AITCS-1 is even stable in aqua regia solution for at least 24 h. The BET specific surface areas of AITCS-1 and -2 are 11 and 1506 m<sup>2</sup>g<sup>−1</sup>, respectively. AITCS-2 takes up 51 cm<sup>3</sup>(STP)g<sup>−1</sup> CO<sub>2</sub> and 15 cm<sup>3</sup>(STP)g<sup>−1</sup> CH<sub>4</sub> at 298 K and 1 bar, which is relatively high among MOF materials. AITCS-1 takes up 30 cm<sup>3</sup>g<sup>−1</sup> CO<sub>2</sub> and 4.2 cm<sup>3</sup>g<sup>−1</sup> CH<sub>4</sub> at 298 K and 1 bar. The rapid and stable photocurrent responses of AITCS-1 and -2 under UV and visible-light illumination are observed. Moreover, AITCS-1 photocatalyzes the water-splitting reaction under visible light with an average hydrogen evolution efficiency of 50 μmolg<sup>−1</sup>h<sup>−1</sup> for the first 10 h in a mixture of water and triethanolamine.

## Introduction

Visible light is the major component (43%) of the inexhaustible and clean solar energy. Metal–organic frameworks (MOFs) can be synthesized as visible-light photocatalysts due to their designability.<sup>[1]</sup> However, relatively low water and thermal stabilities of most MOFs could be the key limitations for their practical applications.<sup>[2]</sup> Al-MOFs show exceptional water and thermal stability. They are relatively light due to the low atomic number of aluminum. Although few Al-MOFs have been reported, they have become of interest for industrial use.<sup>[3]</sup> To the best of our knowledge, only two MOFs have been

promoted to the level of commercial applications. A dense zinc glutarate<sup>[4]</sup> is currently used as an epoxide polymerization catalyst, whereas the microporous aluminum fumarate A520 is employed as a sorbent to store and deliver natural gas for automotive applications.<sup>[3,5]</sup> To date, the total number of structures of Al-MOFs is only 42 (Tables S1 and S2 in the Supporting Information), among which only 16 structures are based on single-crystal XRD analyses (Table S2 in the Supporting Information). Due to the small sizes, 9 of the 16 single-crystal XRD diffractions were performed by using synchrotron radiation, which is not readily accessible to researchers. Therefore, it is necessary to find a general method to obtain single crystals of Al-MOFs for common XRD structure determination. In addition, no tetrahedral-shaped carboxylic acid ligand has been applied in the syntheses of Al-MOFs.

Loiseau et al. first applied an aqueous solution of HF to synthesize single crystals of an Al-MOF (MIL-96) in 2006.<sup>[6]</sup> They also utilized tetraethyl orthosilicate (TEOS) and trimethyl 1,3,5-benzenetricarboxylate, an ester ligand instead of the acid ligand, to facilitate the formation of Al-MOFs. Since then, no single crystals of Al-MOFs have been reported by adding HF acid. The method of adding an aqueous solution of HF to grow large crystals has been applied in related fields. For example, large single crystals of AlPO<sub>4</sub>-34, a molecular sieve, was synthesized by adding an aqueous solution of HF.<sup>[7]</sup> Guo et al. reported that irregular particles of UiO-66, a Zr<sup>IV</sup> carboxylate MOF, were changed into regular-shaped particles and the sizes increased from 0.2–0.5 to 5–10 μm upon adding HF acid.<sup>[8]</sup> Simple organic acids were also applied in the syntheses of

[a] Y. Guo,<sup>+</sup> L.-Z. Dong, Dr. W. Han, Prof. M. Fang, Prof. H.-K. Liu, Dr. Y. Wu, Prof. Y.-Q. Lan

Department of Chemistry, Nanjing Normal University  
Nanjing 210023 (P.R. China)  
E-mail: fangmin@njnu.edu.cn  
wuyong@njnu.edu.cn  
yqlan@njnu.edu.cn

[b] Dr. J. Zhang<sup>+</sup>  
Anhui Key Laboratory of Advanced Building Materials  
Anhui Jianzhu University, Hefei, Anhui 230022 (P.R. China)

[c] Prof. Y. Xu  
State Key Laboratory of Materials-Oriented Chemical Engineering  
Nanjing Tech University, Nanjing 210009 (P.R. China)

[d] Prof. M. Fang, Prof. H.-K. Liu  
State Key Laboratory of Coordination Chemistry  
Nanjing University, Nanjing 210093 (P.R. China)

[<sup>+</sup>] These authors contributed equally to this work.

Supporting information and the ORCID number(s) for the author(s) of this article can be found under <https://doi.org/10.1002/chem.201703682>.

MOF single crystals, especially in the syntheses of Zr-MOFs.<sup>[9]</sup> Despite of this progress, obtaining large single crystals of an Al-MOF is still a difficult task.

Herein, single crystals of the known MIL-53(Al) (previously obtained as powders), and two novel Al-MOF crystals,  $\text{Al}_3(\text{OH})_3(\text{HTCS})_2$  (AITCS-1; TCS = tetrakis(4-oxycarbonylphenyl)silane) and  $[\text{Al}_3\text{O}_2(\text{OH})_3(\text{TCS})_2(\text{H}_2\text{O})_2]$  (AITCS-2), which are large enough for conventional single-crystal diffraction measurements, are obtained by adding an aqueous solution of HF or formic acid. The technique of obtaining those single crystals is likely a general method for obtaining high-quality, large, single crystals of Al-MOFs. The syntheses, structures, chemical and thermal stabilities, gas adsorptions, photocatalytic water splitting, and photoelectric properties of AITCS-1 and -2 are reported. Although the  $\text{H}_4\text{TCS}$  ligand absorbs only UV light, AITCS-1 and -2 absorb visible light; AITCS-1 absorbs more visible light than that of AITCS-2. The band gaps and conduction band (CB) and valence band (VB) edge positions were determined by means of UV/Vis reflectance spectra and an electrochemical (EC) method. AITCS-1 photocatalyzes water splitting with a hydrogen evolution efficiency of  $50 \mu\text{mol g}^{-1} \text{h}^{-1}$  for the first 10 h in a mixture of water and triethanolamine (TEOA; 4:1 v/v).

## Results and Discussion

### Syntheses of large single crystals of MIL-53(Al) and AITCS-1

To obtain single crystals of new Al<sup>III</sup> carboxylate MOFs, we first tried to obtain single crystals of a known Al-MOF, MIL-53(Al). A common  $\text{Al}(\text{NO}_3)_3 \cdot 9\text{H}_2\text{O}$ /benzene-1,4-dicarboxylic acid ( $\text{H}_2\text{BDC}$ )/ $\text{H}_2\text{O}$  molar ratio for the synthesis of MIL-53(Al) powder is 2.0:1:178.<sup>[6]</sup> By simply adding an aqueous solution of HF to the above mixture (Table S7 in the Supporting Information), the particles of MIL-53(Al) increase in size (Figure 1 a and b), and eventually large, block, single crystals of  $0.25 \times 0.14 \times 0.07 \text{ mm}$

(Figure 1 c) are obtained with a  $\text{HF}/\text{H}_4\text{TCS}$  molar ratio of 4.4. The single-crystal structure was determined by means of common single-crystal XRD analysis and was consistent with that determined based on powder X-ray diffraction (PXRD) data (Table S3 and Figures S3 and S4 in the Supporting Information).<sup>[4]</sup> In 2015, Seoane et al. obtained MIL-53(Al) single crystals with sizes of  $0.8 \times 0.9 \times 0.4 \mu\text{m}$ ,<sup>[10]</sup> which were not big enough for structure determination by using a common single-crystal XRD diffractometer.

To synthesize single crystals of a new Al<sup>III</sup>-MOF based on the  $\text{H}_4\text{TCS}$  ligand, the  $\text{L}_9(3^4)$  orthogonal array design approach was applied.<sup>[11]</sup> The  $\text{L}_9(3^4)$  array gives nine representative experiments, considering four influencing factors and three different conditions for each factor. The factors we considered were the molar ratio of  $\text{Al}(\text{NO}_3)_3 \cdot 9\text{H}_2\text{O}$  to  $\text{H}_4\text{TCS}$  (1:1, 1:2, and 1:3), the molar ratio of HF to  $\text{H}_4\text{TCS}$  (0, 1.1, and 2.1), the amounts of water (4.0, 6.0, and 8.0 mL), and the fourth factor was kept as the same (e.g., reaction time). Data for experiments designed by this method are given in Table 1. Other synthetic proce-

**Table 1.** The effect of the amounts of reactants on the syntheses of AITCS-1 by using the nine experiments designed with the  $\text{L}_9(3^4)$  orthogonal array.<sup>[a]</sup>

Entry	Molar ratio of $\text{Al}(\text{NO}_3)_3 \cdot 9\text{H}_2\text{O}/\text{H}_4\text{TCS}/\text{HF}/\text{H}_2\text{O}$	Product (size in mm)
1	1:1:0:2850	powder
2	1:1:1.1:4270	small block crystals of AITCS-1
3	1:1:2.1:5700	long needles (Figure S5 a)
4	2:1:0:4270	powder
5	2:1:1.1:5700	large block crystals of AITCS-1 ( $0.17 \times 0.040 \times 0.030$ ) (Figure 1 d)
6	2:1:2.1:2850	large block crystals of AITCS-1 ( $0.20 \times 0.040 \times 0.020$ )
7	3:1:0:5700	powder
8	3:1:1.1:2850	large block crystals of AITCS-1 ( $0.10 \times 0.050 \times 0.050$ ) (Figure S5 c)
9	3:1:2.1:4270	needles + AITCS-1 block crystals

[a] The amount of  $\text{H}_4\text{TCS}$  (40 mg, 0.078 mmol) was kept constant and the other synthetic procedures and conditions were the same as those used in a the typical synthesis of AITCS-1.

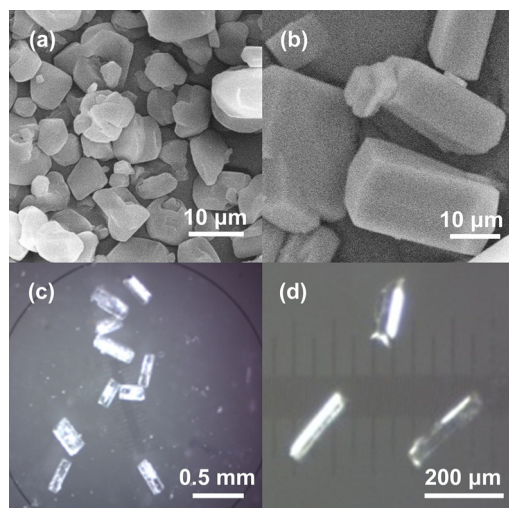


**Figure 1.** Morphologies of large single crystals of MIL-53(Al) (c) and AITCS-1 (d). SEM images of products prepared by using the same procedure as that of the synthesis of MIL-53(Al) single crystals, but with different  $\text{HF}/\text{H}_4\text{TCS}$  molar ratios (0.39 (a) and 2.3 (b)) are also given for comparison.

dures are the same as that used for the synthesis of MIL-53(Al) single crystals, except that the heating and cooling rates of the oven temperature were slowed and controlled. Large, block-shaped single crystals of a new phase were obtained in three experiments (Table 1, entries 5, 6, and 8). One of the crystals was structurally determined to be  $[\text{Al}_3(\text{OH})_3(\text{HTCS})_2]$  (AITCS-1) by single-crystal XRD analysis. The above results demonstrate the efficiency of the orthogonal experimental design method. From only nine experiments, pure, large single crystals of AITCS-1 were harvested and the crystal structure was obtained by using a common single-crystal XRD diffractometer. This systematic analysis tool is widely used in biochemistry and various fields of chemistry;<sup>[12]</sup> however, few reports have been published in the field of coordination networks. By applying formic acid instead of an aqueous solution of HF, we also successfully obtained large single crystals of AITCS-1 by using  $\text{H}_4\text{TCS}$

(10 mg, 0.020 mmol) in each preparation (the overall molar ratio of  $\text{Al}^{3+}/\text{H}_4\text{TCS}/\text{HCOOH}/\text{H}_2\text{O}$  is 3.9–6.5:1:680:17 000; Table S8 and Figures S6 and S7 in the Supporting Information).

### Syntheses of high-quality, large, single crystals of AITCS-2

AITCS-1 has a low porosity of 16.8% due to the pore-filling effect of the  $-\text{COOH}$ -containing arm of each ligand. In the following endeavors, we successfully obtained a novel aluminum carboxylate MOF based on the completely deprotonated  $\text{TCS}^{4-}$  ligand: AITCS-2. Selected experiments and results are given in Table 2; the corresponding PXRD results and pictures of selected crystals given in Figures 2 and 3. In the beginning, we obtained the powder phase of AITCS-2 (Table 2, entry 1). We thought it was a potential target of a new Al-MOF because its PXRD pattern had a peak at a low  $2\theta$  angle of  $6.02^\circ$  (No. 1 in

Table 2. Syntheses of single crystals of AITCS-2. <sup>[a]</sup>		
Entry	Molar ratio of $\text{Al}^{3+}/\text{H}_4\text{TCS}/\text{HCOOH}/\text{DMF}/\text{H}_2\text{O}^{[b]}$	Products (size in mm)
1 <sup>[d]</sup>	4.0 (293 mg):1.0 (10):680 (0.50):2660 (4.0):0	AITCS-2, powder
2 <sup>[c]</sup>	6.0 (351):1.0 (30):226 (0.5):443 (2):0	AITCS-2, powder
3	6.0 (234):1.0 (20):374 (0.55):670 (2):0	phase C, glassy particles
4	5.8 (227):1.0 (20):340 (0.5):670 (2):0	phase C, rhombic crystals, (0.040×0.030×0.010) (Figure S8)
5 <sup>[c]</sup>	6.0 (234):1.0 (20):340 (0.5):670 (2):0	AITCS-2, rhombic single crystals
6	6.0 (117):1.0 (10):680 (0.5):1990 (3):0	AITCS-2, rhombic single crystals (0.14×0.10×0.040)
7 <sup>[c]</sup>	6.0 (117):1.0 (10):1090 (0.8):1990 (3):0	phase D, glassy particles
8 <sup>[e]</sup>	5.8 (227):1.0 (20):340 (0.5):670 (2):0	AITCS-2, rhombic single crystals (0.15×0.10×0.030)
9	5.8 (227):1.0 (20):270 (0.4):500 (1.5):710 (0.5)	AITCS-2, block-like single crystals (0.20×0.10×0.030)
10 <sup>[c]</sup>	5.8 (227):1.0 (20):270 (0.4):500 (1.5):710 (0.5)	AITCS-2, block-like single crystals (0.28×0.12×0.045)
11	5.8 (227):1.0 (20):310 (0.45):500 (1.5):710 (0.5)	AITCS-2, block-like single crystals (0.20×0.10×0.020)
12 <sup>[d]</sup>	5.8 (227):1.0 (20):310 (0.45):500 (1.5):710 (0.5)	AITCS-2, block-like single crystals (0.15×0.08×0.020)
13	5.8 (227):1.0 (20):270 (0.4):470 (1.4):850 (0.6)	AITCS-2, block-like single crystals (0.20×0.10×0.020)
14 <sup>[d]</sup>	5.8 (227):1.0 (20):270 (0.4):470 (1.4):850 (0.6)	AITCS-2, block-like single crystals (0.08×0.030×0.015)

[a] PXRD patterns are given in Figure 2 and pictures of selected products are given in Figure 3. [b] Data in parentheses are the amount of  $\text{Al}(\text{NO}_3)_3\text{aq}$  (1.0 M, mL; except for entry 1, in which solid  $\text{Al}(\text{NO}_3)_3\cdot 9\text{H}_2\text{O}$  was applied),  $\text{H}_4\text{TCS}$  (mg),  $\text{HCOOH}$  (mL),  $\text{DMF}$  (mL), and  $\text{H}_2\text{O}$  (mL). The total volume of  $\text{DMF}$  and  $\text{H}_2\text{O}$  is 2.0 mL, except for entry 1, in which 4 mL of  $\text{DMF}$  was applied; the temperature of the oven was raised from room temperature to  $120^\circ\text{C}$  with a  $1.0^\circ\text{Cmin}^{-1}$  heating ramp, kept at  $120^\circ\text{C}$  for 3 d, and then cooled to  $25^\circ\text{C}$  at a rate of  $10.0^\circ\text{Ch}^{-1}$ . [c] Same conditions as those given in [b], except that the cooling rate was  $2.0^\circ\text{Ch}^{-1}$  to  $25^\circ\text{C}$ . [d] The autoclave was put into an oven, and the temperature of the oven was increased from 25 to  $120^\circ\text{C}$  naturally, kept at  $120^\circ\text{C}$  for 3 d, and then cooled to room temperature naturally. [e] Reaction temperature was  $130^\circ\text{C}$ ; the heating ramp and cooling rate were the same as those given in [b].

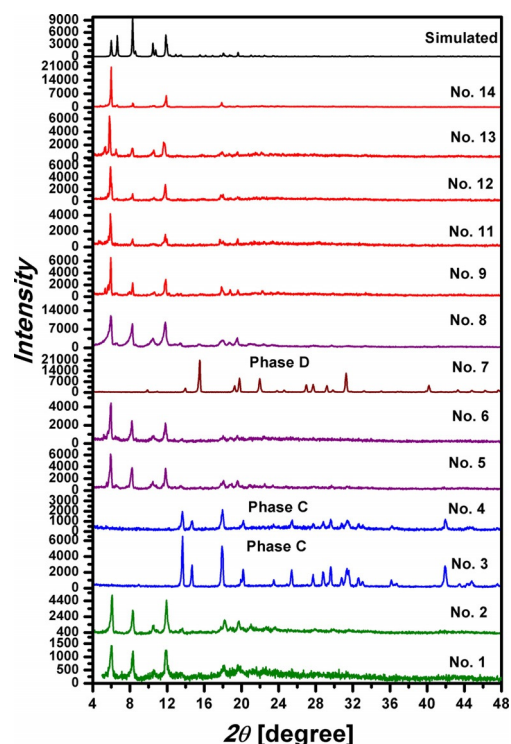


Figure 2. PXRD patterns of AITCS-2, phase C, and phase D produced from experiments given in Table 2, compared with the simulated PXRD patterns based on the cif file of AITCS-2 obtained by using Mercury software.

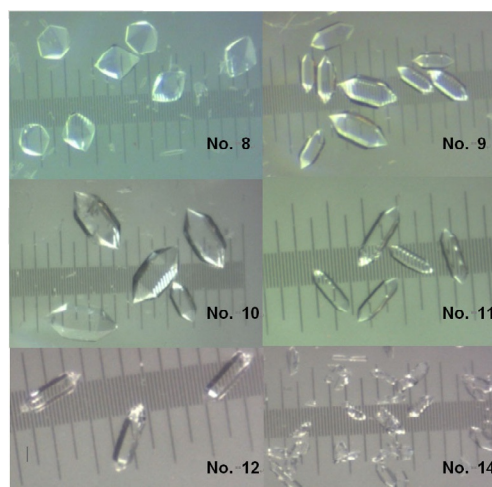


Figure 3. Pictures of the AITCS-2 single crystals synthesized by the experiments given in Table 2. The length of the minimum grade in the pictures is 0.01 mm.

Figure 2), which was smaller than that of the first PXRD peak of AITCS-1 ( $6.63^\circ$ ), and suggested it might have bigger pores than those in AITCS-1. Subsequently, in a more concentrated solution and with a slower heating and cooling rate of the oven, powders of higher crystallinity (No. 2 in Figure 2) were obtained, as indicated by the intensity increase of the peak at  $6.02^\circ$  (from 1500 to 4500). Based on No. 2 in Figure 2, by increasing the acidity of the system, using a more dilute reactant



mixture, and a faster cooling rate, rhombic crystals were obtained (Table 2, entries 5 and 6); however, the crystallinity was low (Figure 2). By raising the temperature from 120 to 130 °C, we obtained perfect-looking, large, rhombic crystals (0.15 × 0.10 × 0.030 mm; No. 8 in Figure 3). The PXRD diffraction intensity of the peak at 6.02° is high, but the peaks are broad, which indicates that there is disorder in the crystals causing broadening of the peaks. Only a few or no single-crystal XRD diffraction points were observed from all rhombic crystals obtained in DMF. Increasing the acidity of the system and cooling rate (10 °C h<sup>-1</sup>) resulted in a dense phase (phase C, Nos. 3 and 4 in Figure 2). This phase can also be obtained as rhombic crystals (No. 4, Figure S8 in the Supporting Information). Even higher acidity resulted in another dense phase (phase D, No. 7 in Figure 2).

To grow better-quality crystals of AITCS-2, we then changed the polarity of the solvent by using a mixture of DMF and H<sub>2</sub>O. The total amount of solvent was kept at 2.0 mL to maintain the concentration. Block-like crystals were obtained in this system (Table 2, entries 9–14, and Figures 2 and 3). Contrary to our expectations, increasing the cooling rate increased the crystallinity of AITCS-2 (No. 14 versus No. 13; No. 12 versus No. 11 in Figure 2). The diffraction intensity of the peak at 6.02° of product No. 14 (Figure 2) reaches 21000 and the peaks are very sharp. Only with single crystals from this experiment did we obtain good diffraction data with a qualified resolution and the single-crystal structure of AITCS-2 was solved. Data obtained from other block-like crystals all have poor resolutions (> 1.0). Tsao et al. also found that high-quality MOFs could be synthesized as the cooling rate increased.<sup>[13]</sup> In the synthesis of AITCS-1, we also found that a faster cooling rate increased its crystallinity (Figure S17 in the Supporting Information).

The position of the simulated PXRD pattern of AITCS-2 based on the crystal structure is consistent with the observed patterns; however, the intensities are different (Figure 2). This could be because the crystal for structure determination was measured with solvents inside the pores; however, the ob-

served PXRDs were obtained after the samples were dried at 60–90 °C for 12 h. The peak intensities of the PXRD pattern of a sample soaked in water for 3 d (Figure 7b, below) are more consistent with the simulated PXRD pattern based on the crystal structure. These phenomena have been observed by us and others.<sup>[14]</sup> Intensity differences between observed patterns are probably due to different orientation preferences of prepared AITCS-2 because we have prepared them in different shapes. Some small additional peaks at low angles are probably due to small amounts of impurities.

## Structures of AITCS-1 and -2

The minimum unsymmetrical units of AITCS-1 and -2 are given in Figure S9 in the Supporting Information. Single-crystal XRD analysis reveals that AITCS-1 has a 3D framework and crystallizes in the monoclinic space group *C2/c* (Table S3 in the Supporting Information). The coordination environments of the ligand and metal ions of AITCS-1 are shown in Figure 4a. The carboxylate groups all act as bidentate ligands that bridge two adjacent Al<sup>III</sup> ions. Six coordinated Al<sup>3+</sup> ions (Al1 and Al2) are bridged by carboxylate groups and OH<sup>-</sup> groups to form zigzag planar chains along the *c* axis, as shown in Figure 4b. Twenty-nine of the total 42 Al-MOF structures contain 1D metal oxide chains (Tables S1 and S2 in the Supporting Information). However, only MIL-96<sup>[6]</sup> and 467-MOF<sup>[15]</sup> contain the same zigzag chains as those in AITCS-1. The chains are connected by HTCS<sup>3-</sup> ligands to form a 3D framework, which contains rhombic channels of 6.4(4.7) × 9.1(7.4) Å<sup>[41]</sup> along the *c* axis (Figure 4c and Figure S10 in the Supporting Information). The unprotonated arm of H<sub>4</sub>TCS fills the pores of AITCS-1, which gives it a small porosity of 16.8% (probing radius: 1.2 Å) and a solvent-accessible volume/unit cell of 995.2 Å<sup>3</sup>, as calculated by the PLATON program.<sup>[16]</sup> The pore volume calculated based on the above data is 0.13 cm<sup>3</sup> g<sup>-1</sup>. Based on topology analysis by using the ToposPro program,<sup>[17]</sup> the 3D framework of AITCS-1 can be simplified to a 3-nodal 6,6,6-c net (Si<sub>2</sub>(Al1)(Al2)<sub>2</sub>), with a

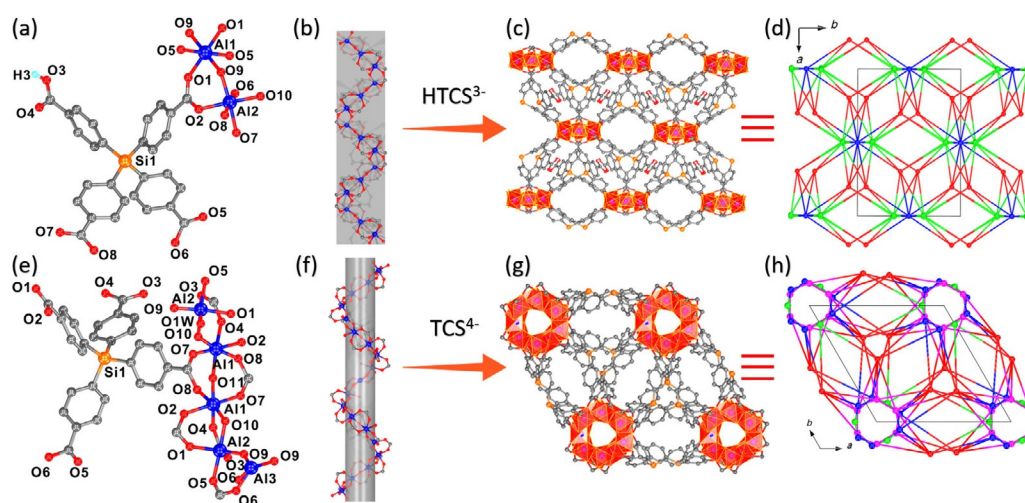


**Figure 4.** The structures of AITCS-1 (a–d) and AITCS-2 (e–h). The coordination environments (a and e), the Al<sup>3+</sup> chains (b and f), packings along the *c* axis (c and g), and the topologies (d and h) are given.

point symbol of  $(3^3 4^2 5^7 6^3)_2 (3^4 4^2 5^2 6^4 7^2 8) (3^4 4^4 5^4 6^3)_2$ , as shown in Figure 4d. To the best of our knowledge, this is a new topology.

Single-crystal XRD analysis reveals that AITCS-2 is a 3D framework, crystallizes in the trigonal space group  $P3_1 2_1$  (Table S4 in the Supporting Information). All carboxylate groups act as bidentate ligands, bridging two adjacent  $\text{Al}^{\text{III}}$  ions, as in AITCS-1.  $\text{Al}^{3+}$  ions ( $\text{Al1}$ ,  $\text{Al2}$ , and  $\text{Al3}$ ) are all six-coordinated and bridged by carboxylate groups,  $\text{O}^{2-}$  ( $\text{O9}$ ),  $\text{OH}^-$  ( $\text{O1H}$  and  $\text{O10}$ ), and  $\text{H}_2\text{O}$  ( $\text{O1w}$ ) groups (Figure 4e) to form spiral chains along the  $c$  axis, as shown in Figure 4f. To the best of our knowledge, this spiral-shaped aluminum oxide chain is a new type of substructural building unit (SBU) for Al-MOFs. In contrast, the zigzag aluminum oxide chains in AITCS-1 are planar. Each  $\text{TCS}^{4-}$  ligand connects with three  $\text{Al}^{3+}$  chains, as shown in Figure S11 in the Supporting Information, to form a 3D framework with elliptical channels of  $4.6(3.0) \times 9.4(7.7) \text{ \AA}^{[41]}$  (channels shown in the  $a$  and  $b$  direction),  $7.5(5.9)$ , and  $10.4(8.7) \times 5.8(4.0) \text{ \AA}^{[41]}$  (channels shown in the  $c$  direction; Figure 4g and Figure S10 in the Supporting Information). It has a large porosity of 57.4% (probing radius:  $1.2 \text{ \AA}$ ) and the solvent-accessible volume/unit cell is  $4449 \text{ \AA}^3$ , as calculated by the PLATON program.<sup>[16]</sup> The pore volume calculated based on the above data is  $0.70 \text{ cm}^3 \text{ g}^{-1}$ . Based on topology analysis by using the ToposPro program,<sup>[17]</sup> the 3D framework of AITCS-2 can be simplified to a 4-nodal 4,5,6,8-c net ( $\text{Si}_2 (\text{Al1})_2 (\text{Al2})_2 (\text{Al3})$ ) with a point symbol of  $(3^4 4^7 5^{12} 6^5)_2 (3^4 4^5 5^4 6^3)_2 (3^3 4^3 5^3 6)_2 (3^2 4^1 5^2 6)$ , as shown in Figure 4h. To the best of our knowledge, this is a new topology.

## Adsorption properties of AITCS-1 and 2

AITCS-1 absorbed a very limited number of  $\text{N}_2$  and  $\text{H}_2$  molecules at 77 K, as shown in Figure S12 in the Supporting Information, which is consistent with its small porosity. The Langmuir specific surface area is  $12.1 \text{ m}^2 \text{ g}^{-1}$  (BET:  $11 \text{ m}^2 \text{ g}^{-1}$ ) based on the nitrogen adsorption isotherm at 77 K. In the region of  $P/P_0 > 0.70$ , the isotherm began to increase sharply, which indicated the presence of some textural mesopores.<sup>[18]</sup> The  $\text{H}_2$  uptake is  $29.4 \text{ mL g}^{-1}$  ( $1.31 \text{ mmol g}^{-1}$ ,  $0.26 \text{ wt\%}$ ) under 1 bar at 77 K. The  $\text{CO}_2$  uptakes at 273 and 298 K under 1 atm are 38 and  $30 \text{ mL g}^{-1}$  ( $1.70$  and  $1.34 \text{ mmol g}^{-1}$ ;  $7.5$  and  $5.9 \text{ wt\%}$ ), respectively; and increased to 112 and  $97 \text{ mL g}^{-1}$  ( $5.0$  and  $4.3 \text{ mmol g}^{-1}$ ;  $22$  and  $19 \text{ wt\%}$ ) under 9 atm (Figure S12 in the Supporting Information). The  $\text{CH}_4$  uptakes at 273 and 298 K under 1 atm are  $6.1$  and  $4.2 \text{ mL g}^{-1}$  ( $0.27$  and  $0.19 \text{ mmol g}^{-1}$ ;  $0.44$  and  $0.30 \text{ wt\%}$ ), respectively, and increased to 35 and  $26 \text{ mL g}^{-1}$  ( $1.56$  and  $1.16 \text{ mmol g}^{-1}$ ;  $2.5$  and  $1.9 \text{ wt\%}$ ) under 9 atm. Thus, AITCS-1 absorbs more  $\text{CO}_2$  than  $\text{CH}_4$ , which suggests it might be applied to remove  $\text{CO}_2$  from natural gas. The uptake amount of  $\text{CO}_2$  is high, considering its low pore volume ( $0.13 \text{ mL g}^{-1}$ ).<sup>[19]</sup> We observed hystereses in these sorption experiments (Figure S12 in the Supporting Information). MOFs with pores of diameters less than  $10 \text{ \AA}$  could result in hysteresis phenomena due to their small pore nature, as reported by Kim et al.<sup>[20]</sup>

The permanent porosity of AITCS-2 was confirmed by nitrogen and hydrogen sorption experiments at 77 K (Figure 5). The  $\text{N}_2$  uptake is  $385 \text{ cm}^3 (\text{STP}) \text{ g}^{-1}$ , the BET specific surface area is  $1506 \text{ m}^2 \text{ g}^{-1}$ , the Langmuir surface area is  $1642 \text{ m}^2 \text{ g}^{-1}$ , and the pore volume is  $0.55 \text{ cm}^3 \text{ g}^{-1}$ . The type I adsorption curve suggests the microporous nature of AITCS-2. The  $\text{H}_2$  uptake is  $201 \text{ mL g}^{-1}$  ( $1.79 \text{ wt\%}$ ) under 1 bar at 77 K, which is moderate among MOF materials. For example, ZIF-8 (BET:  $1630 \text{ m}^2 \text{ g}^{-1}$ ) absorbs  $1.27 \text{ wt\%}$ , MOF-5 (BET:  $3362 \text{ m}^2 \text{ g}^{-1}$ ) absorbs  $1.32 \text{ wt\%}$  under 1 bar at 77 K.<sup>[21]</sup> The  $\text{CO}_2$  and  $\text{CH}_4$  uptakes at 298 K and 1 bar are 51 ( $2.3 \text{ mmol g}^{-1}$ ,  $10 \text{ wt\%}$ ) and  $15 \text{ cm}^3 (\text{STP}) \text{ g}^{-1}$  ( $0.67 \text{ mmol g}^{-1}$ ,  $1.1 \text{ wt\%}$ ), respectively. The  $\text{CO}_2$  and  $\text{CH}_4$  uptakes increase to 92 ( $4.1 \text{ mmol g}^{-1}$ ,  $18 \text{ wt\%}$ ) and  $27 \text{ cm}^3 (\text{STP}) \text{ g}^{-1}$  ( $1.2 \text{ mmol g}^{-1}$ ,  $2.0 \text{ wt\%}$ ) at 273 K and 1 bar. To the best of our knowledge, the  $\text{CO}_2$  and  $\text{CH}_4$  adsorption capacities of AITCS-2 are relatively high among the reported values of known MOFs measured under the same conditions.<sup>[19c, 22]</sup> UiO(bpdc) (a Zr-MOF based on the 2,2'-bipyridine-5,5'-dicarboxylate (bpdc) ligand) was recently reported as a material

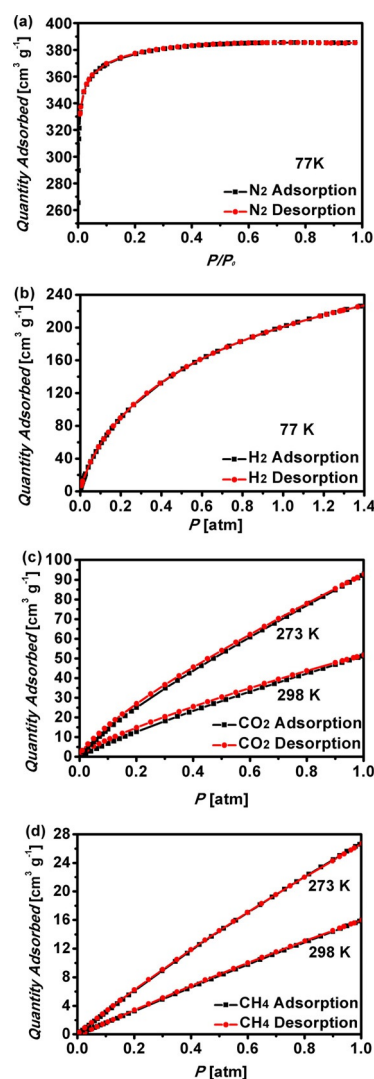


Figure 5.  $\text{N}_2$  (77 K),  $\text{H}_2$  (77 K),  $\text{CO}_2$  (273 and 298 K), and  $\text{CH}_4$  (273 and 298 K) adsorption/desorption isotherms of AITCS-2.

with high CO<sub>2</sub> and CH<sub>4</sub> uptakes.<sup>[23]</sup> The CO<sub>2</sub> and CH<sub>4</sub> uptakes of AITCS-2 are higher than that of UiO(bpdC), which has a much larger BET surface area (2646 m<sup>2</sup> g<sup>-1</sup>) and absorbs 8.0 wt% CO<sub>2</sub> or 1.0 wt% CH<sub>4</sub> at 1 bar and 293 K, and 13.0 wt% CO<sub>2</sub> at 1 bar and 273 K.<sup>[23]</sup>

### IR and Raman spectra of AITCS-1 and -2

The IR and Raman spectra of AITCS-1 and -2 are very similar (Figure S14 in the Supporting Information), which is consistent with the fact that they have similar bonds in the frameworks. When the CuBTC MOF (BTC = 1,3,5-benzene tricarboxylate) was subjected to a high-humidity environment, the most notable changes in the IR spectra were the gradual appearance of bands at  $\tilde{\nu}$  = 1708 and 1243 cm<sup>-1</sup>, which were assigned to the C=O and C–O stretching bands of the COOH group.<sup>[24]</sup> Based on this finding, the sharp band at  $\tilde{\nu}$  = 3690 cm<sup>-1</sup> and the strong bands at  $\tilde{\nu}$  = 1704 and 1286 cm<sup>-1</sup> in the IR spectrum of AITCS-1 were assigned to the free OH of COOH stretching, C=O (usually very strong), and C–O stretching modes of the COOH group, respectively, which were absent in the IR spectrum of AITCS-2; this is consistent with the fact that AITCS-2 does not contain a –COOH group. Because the IR intensity of  $\nu_{\text{sym}}(\text{COO}^-)$  is usually weaker than the IR intensity of  $\nu_{\text{asym}}(\text{COO}^-)$ , the bands at  $\tilde{\nu}$  ≈ 1610 and 1385 cm<sup>-1</sup> in the IR

spectra of AITCS-1 and -2 were assigned to the  $\nu_{\text{asym}}(\text{COO}^-)$  and  $\nu_{\text{sym}}(\text{COO}^-)$  modes, respectively.

### Water and thermal stability of AITCS-1 and -2

Thermogravimetric (TG) curves of AITCS-1 and -2 are given in Figure 6. The weight losses of 2.3 (AITCS-1) and 2.4% (AITCS-2) before 200 °C are due to the release of adsorbed water molecules. The second weight loss of 6.2% in the TG of AITCS-1 occurred in the range of 230 to 390 °C; this corresponded to decomposition of the framework, which was consistent with the fact that it completely lost crystallinity after being heated at 400 °C for 4 h (Figure 7a). However, PXRD (Figure 7a) and IR (Figure S15 in the Supporting Information) studies indicate that the framework remained intact, even after being heated at 350 °C for 4 h.

The second weight loss of 3.6% observed in the TG curve of AITCS-2 (Figure 6) occurred in the range of 257–320 °C, which was assigned to the loss of coordinated water (theoretical amount: 2.8%). PXRD (Figure 7b) studies indicate that the framework remained intact, even after being heated at 350 °C for 4 h. The IR spectra of the sample heated at 250–350 °C (Figure S15 in the Supporting Information) indicate that AITCS-2 gradually decomposes at temperatures above 250 °C, as suggested by the increase of the band intensities due to the formation of the –COOH group at  $\tilde{\nu}$  = 1707 (C=O stretching) and 1263 cm<sup>-1</sup> (C–O stretching; Figure S15i in the Supporting Information). AITCS-1 and -2 are stable over wide pH range (1–11) for at least 24 h (Figure 7), and AITCS-1 is even stable in aqua regia solution for 24 h without the loss of crystallinity, as indicated by the PXRD pattern (Figure 7) and IR and Raman spectra (Figure S14 in the Supporting Information). In contrast, aqua regia destroys AITCS-2. Thus, AITCS-1 shows greater chemical and thermal stability than that of AITCS-2; this could be due to its low porosity.

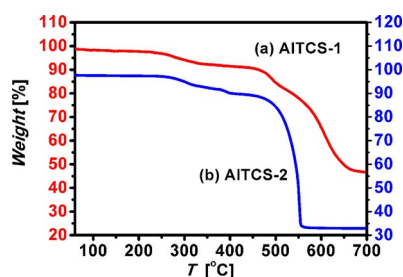


Figure 6. TG curves of AITCS-1 and -2.

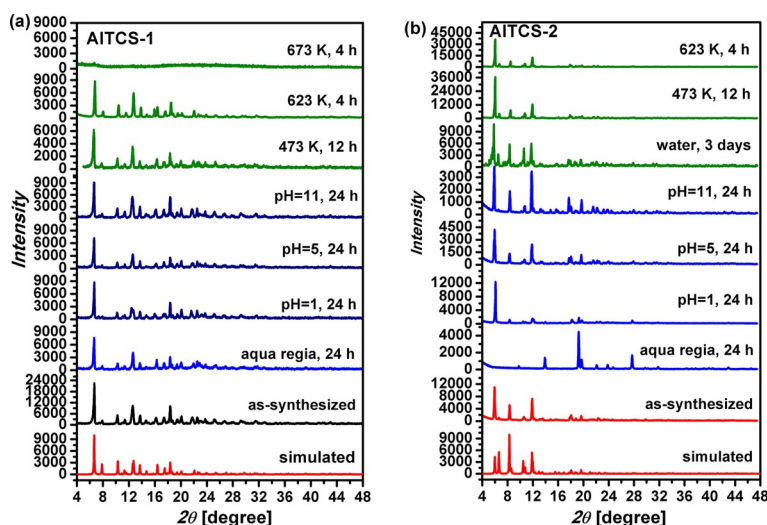
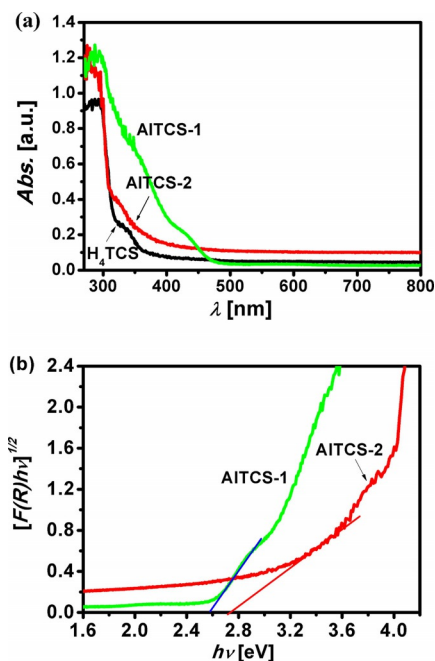


Figure 7. Thermal and water stabilities of AITCS-1 (a) and AITCS-2 (b) checked by PXRD.



## UV/Vis diffuse reflectance spectra of AITCS-1, AITCS-2, and the H<sub>4</sub>TCS ligand

The UV/Vis diffuse reflectance spectra of H<sub>4</sub>TCS, AITCS-1, and AITCS-2, in the form of absorption coefficient versus wavelength, are given in Figure 8 (the plot of percentage *R* versus wavelength are given in Figure S16 in the Supporting Information). The ligand H<sub>4</sub>TCS basically only absorbs UV light, where-



**Figure 8.** Optical properties of AITCS-1 and -2. a) UV/Vis reflectance spectra of H<sub>4</sub>TCS, AITCS-1, and AITCS-2 in the form of absorbance versus wavelength. b) The band gaps of AITCS-1 and -2 determined by plotting  $[F(R)hv]^{1/2}$  versus  $hv$ .

as AITCS-1 and -2 can absorb visible light and the absorbance of AITCS-1 is greater than that of AITCS-2. The above results demonstrate that Al<sup>3+</sup>, which is not an electron-rich ion, could also decrease the band gaps of MOFs to allow them to absorb visible light. This function of Al<sup>3+</sup> has not been recognized. Lu et al. proposed that the band gaps of semiconducting MOFs could be decreased by applying electron-rich metal nodes based on limited experimental and theoretical results.<sup>[1b]</sup> A possible explanation for the absorbance difference between AITCS-1 and -2 is given below.

A structural motif, namely, donor- $\pi$  bridge-acceptor (organic  $\pi$  systems end-capped with an electron donor (D) and an electron acceptor (A)), is widely applied in the design of efficient organic dyes applied in dye-sensitized solar cells (DSSCs).<sup>[25]</sup> Due to the D-A interaction, or intramolecular charge transfer (ICT), a new low-energy molecular orbital (MO) is formed. Facile excitation of electrons within the new MO can be achieved by using visible light.<sup>[25c]</sup> For example, whereas aniline and nitrobenzene only absorb in the UV region, 4-nitroaniline shows an intense and bathochromically shifted long-wavelength absorption maxima (charge-transfer (CT) band),

and absorbs in the visible-light region. On the contrary, 3-nitroaniline showed only a diminished CT band, as a result of a nonconjugating arrangement of the amino donor and nitro acceptor.<sup>[25c]</sup> AITCS-1 can be viewed as a D- $\pi$ -A system due to its unsymmetrical structure, which is caused by its carboxyl groups. The -SiR<sub>3</sub> group can be seen as the electron donor, the phenyl ring is the  $\pi$  bridge, and -COOH is the electron acceptor; thus it starts to absorb visible light. In contrast, the symmetric structure of AITCS-2 does not make it a D- $\pi$ -A system, and thus, it absorbs little visible light.

The band gaps of materials can be calculated from Equation (1):<sup>[26]</sup>

$$\alpha hv = A(hv - E_g)^{n/2} \quad (1)$$

in which  $\alpha$ ,  $v$ ,  $E_g$ , and  $A$  are the absorption coefficient, light frequency, band gap, and a constant, respectively;  $n$  is determined by the optical transition type of the semiconductor (i.e.,  $n$  equals 1 for a direct, allowed transition and 4 for an indirect, forbidden transition)<sup>[26a]</sup> Because  $\alpha$  is proportional to  $F(R)$  ( $F(R)$  equals  $(1-R)^2/(2R)$ , in which  $R$  is the reflectance in the UV/Vis diffuse reflectance spectra),<sup>[26c,d]</sup> the energy intercept of a plot of  $[F(R)hv]^2$  versus energy ( $hv$ ) yields  $E_g$  for a direct, allowed transition if the linear region is extrapolated to zero coordinate, and the energy intercept of a plot of  $[F(R)hv]^{1/2}$  versus energy ( $hv$ ) yields  $E_g$  for an indirect, allowed transition. The band gaps of AITCS-1 and -2 are determined as 2.59 and 2.72 eV, respectively, assuming they are indirect band gap semiconductors, or 3.10 or 3.59 eV, respectively, assuming they are direct band gap semiconductors (Figure S16b in the Supporting Information).

## Determination of band gaps and CB and VB edges of AITCS-1 and -2 by an EC method

To determine whether they are direct or indirect band gap semiconductors, the CB edge (LUMO) and VB edge (HOMO) positions of materials were also determined by an EC method, that is, the linear potential scan method, which can be viewed as partial cyclic voltammetry curves. This method is well established in the literature.<sup>[27]</sup> The first oxidation potential ( $E_{ox}$ ) and the first reduction potential ( $E_{red}$ ) can be observed by separate cathodic and anodic scans, respectively, and equal the energy levels of the HOMO (the CB edge) and LUMO (the VB edge) of the material, respectively. The band gap is the difference between  $E_{ox}$  and  $E_{red}$ . However, both potentials were not always observed,<sup>[27c]</sup> which is probably due to the redox reactions of electrolytes during the processes. We therefore, different from reports in the literature, used two different electrolytes (phosphate-buffered saline (PBS; 0.1 M, pH 7.4) and an aqueous solution of H<sub>2</sub>SO<sub>4</sub> (pH 5.01)), so that we could observe both redox potentials and cross-check the results.<sup>[28]</sup> When determining the band edges, the current curves (in red) of the electrolytes obtained by using unmodified indium tin oxide (ITO) electrodes under the same scanning conditions were compared with the observed current curves obtained by using the modified ITO electrodes, as shown in Figure 9 (AITCS-1) and Figure S2 in

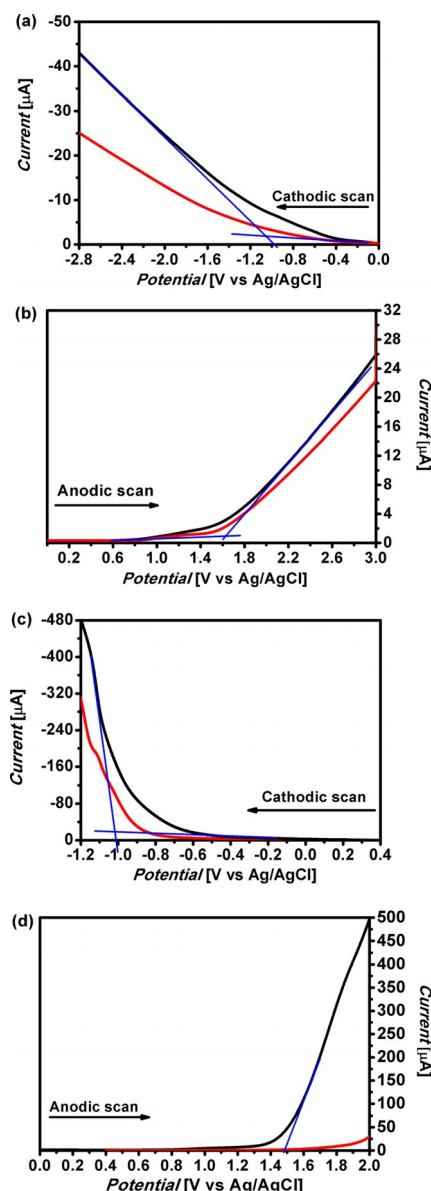


**Figure 9.** Cathodic and anodic linear potential scans for determining the positions of the CB and VB edges of AITCS-1 using two different electrolytes. The red curves are the currents of the electrolytes using the unmodified ITO electrodes (a)–(b): the pH 5.01  $\text{H}_2\text{SO}_4$  aqueous solution, (c)–(d): a phosphate buffered saline (PBS, 0.1 M, pH 7.4).

the Supporting Information (AITCS-2), to distinguish the redox positions of the materials from those of the electrolytes. As shown in Figure 9, the VB band edge of AITCS-1 (1.48 V) was more clearly observed in the anodic scan with PBS (0.1 M, pH 7.4), and the CB band edge of AITCS-1 (−1.06 V) was more clearly observed in the cathodic scan with the aqueous solution of  $\text{H}_2\text{SO}_4$  at pH 5.01. The VB band edge of AITCS-2 (1.58 V) was found in the anodic scan with PBS (0.1 M, pH 7.4), and the CB band edge of AITCS-2 (−0.96 V) was found in the cathodic scan with the aqueous solution of  $\text{H}_2\text{SO}_4$  at pH 5.01 (Figure S2 in the Supporting Information). In other words, the CB and VB potentials are −0.86 and 1.68 V, respectively, for AITCS-1; and −0.76 and 1.78 V, respectively, for AITCS-2 versus the normal

hydrogen electrode (NHE). The band gaps of both AITCS-1 and -2 were 2.54 eV, as determined by the EC method; these are very close to the values determined based on UV/Vis reflectance spectra, assuming they are indirect band gap semiconductors. Thus, both AITCS-1 and -2 are indirect band gap semiconductors.

### Photoelectric properties of AITCS-1 and -2

The photoelectrical properties of AITCS-1 and -2 were studied in a three-electrode setup. Rapid and stable photocurrent responses of AITCS-1 and -2 under UV and visible-light illumination are observed (Figure 10). The anodic photocurrent re-

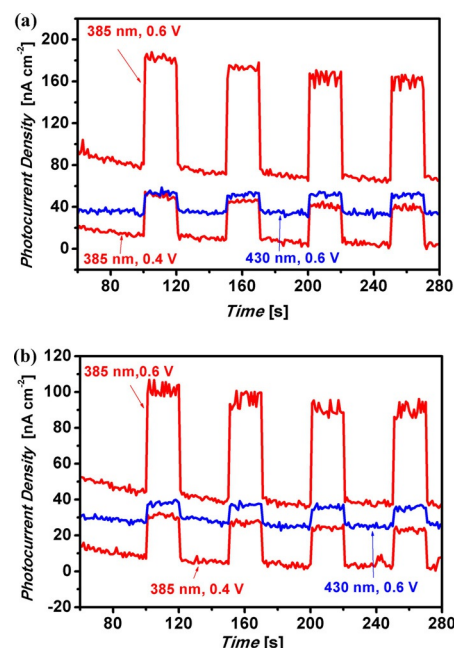


**Figure 10.** AITCS-1 (a) and -2 (b) illuminated with  $\lambda = 385$  and 430 nm light at 0.4 and 0.6 V.

sponse indicates the n-type semiconductor characteristics of these two materials.<sup>[29]</sup> The current increases upon irradiation at shorter wavelength, which is consistent with the higher light absorbances of AITCS-1 and -2 at shorter wavelength, relative to those at longer wavelength. A similar phenomenon was also reported by Ardo et al.<sup>[30]</sup> The generated photocurrent increases with increasing applied bias potential. Such phenomena of other materials were also observed by Zhang et al.<sup>[31]</sup> Under the illumination of 385 nm light, the photocurrent densities of AITCS-1 and -2 reach 100 and 60  $\text{nA cm}^{-2}$ , respectively, at 0.6 V (vs. Ag/AgCl). A higher photocurrent density often means a higher ability to separate the photogenerated electrons and holes.<sup>[29b,32]</sup> The above results suggest that faster recombinations of photogenerated electrons and holes occur under lower potential bias.<sup>[33]</sup> Under the same conditions, the photocurrent intensity increases in the order of AITCS-2 < AITCS-1, which is consistent with the fact that AITCS-1 absorbs more UV and visible light than that of AITCS-2, which suggests



that AITCS-1 has more efficient separation of photogenerated electron–hole pairs.<sup>[32b]</sup>

### Photocatalytic water splitting with AITCS-1

The CB and VB band-edge positions suggest that AITCS-1 and -2 could have applications as visible-light photocatalysts for water splitting based on the known photocatalytic mechanism,<sup>[34]</sup> because the positions of the redox potentials of neutral water are  $-0.41$  and  $0.82$  V for  $E^0(\text{H}^+/\text{H}_2)$  and  $E^0(\text{O}_2/\text{H}_2\text{O})$ , respectively. However, no photocatalytic water-splitting properties of AITCS-1 and -2 were observed in neutral water under visible light, probably due to the low visible-light absorbance and poor photogenerated charge (electrons and holes) separation efficiencies. When 10 mg AITCS-1 (synthesized by the typical synthesis of AITCS-1, which applied a rather slow cooling rate) was put into a mixture of water and TEOA (4:1 v/v, pH 11.0, 100 mL), the evolved hydrogen reached a maximum of  $500 \mu\text{mol g}^{-1}$  after 10 h with an average rate of  $50 \mu\text{mol g}^{-1} \text{h}^{-1}$  under visible light ( $\lambda = 420\text{--}800$  nm). TEOA acts as a sacrificial electron donor, and the reduction potential of  $E^0(\text{TEOA}^+/\text{TEOA})$  equals  $0.82$  [Eq. (2)].<sup>[35]</sup> The TEOA molecules donate electrons to the VB to eliminate holes generated by visible light, and thus, increase the charge separation efficiency (Figure 10b). The reduction potential of  $E^0(\text{H}^+/\text{H}_2)$  at pH 11.0 is  $-0.65$  V [Eq. (3)] ( $E^0$  is the reduction potential in pH 11.0 aqueous solution); thus the photogenerated electrons in the CB of AITCS-1 can reduce  $\text{H}^+$  into  $\text{H}_2$  (Figure 11b). The kinetics of the half-reaction, in which  $\text{H}_2\text{O}$  donates electrons to the CB and itself is oxidized to  $\text{O}_2$  [Eq. (4)], is rather slow and it was not observed. The amount of evolved hydrogen decreases after 10 h, which is probably due to the gradual deterioration of AITCS-1, as indicated by the decreased crystallinity of the recovered solid shown by the PXRD pattern (Figure S17 in the

Supporting Information). Because a portion of gas in the reaction vessel is extracted every hour for analysis, if the hydrogen production is too slow or stops, the apparent hydrogen production decreases. Under the same reaction conditions as those used for AITCS-1, AITCS-2 did not show photocatalytic water-splitting properties under visible light, probably due to its very low visible-light absorbance; and no hydrogen was observed under UV and visible light (300 W Xe lamp without a filter).



The hydrogen evolution efficiency of AITCS-1 is better than the efficiency of the rhodamine B/UiO-66(Zr) reported by Yan et al.,<sup>[36]</sup> which reached a maximum ( $170 \mu\text{mol g}^{-1}$ ,  $34 \mu\text{mol g}^{-1} \text{h}^{-1}$ ) after 5 h under similar reaction conditions. However, it is less efficient than that of Al-PMOF,<sup>[2]</sup>  $[\text{Al}_2(\text{OH})_2(\text{H}_2\text{TCPP})]$  ( $200 \mu\text{mol g}^{-1} \text{h}^{-1}$ ;  $\text{H}_2\text{TCPP}$  = *meso*-tetra(4-carboxylphenyl)porphyrin), and MOF-253-Pt<sup>[37]</sup> ( $4680 \mu\text{mol g}^{-1} \text{h}^{-1}$ , MOF-253:Al(OH)(bpydc), bpydc = 2,2'-bipyridine-5,5'-dicarboxylate) under visible light. To the best of our knowledge, one of the best performing MOF-related materials is the  $\text{MoS}_2/\text{UiO-66}/\text{CdS}$  composite, which could produce  $32500 \mu\text{mol g}^{-1} \text{h}^{-1}$  hydrogen under visible light. Bao et al. reported that a nanocrystalline CoO photocatalyst could carry out overall water splitting, with a hydrogen production efficiency of  $71429 \mu\text{mol g}^{-1} \text{h}^{-1}$ , without the use of a sacrificial agent under the illumination of an AM 1.5 G solar simulator.<sup>[38a]</sup> To the best of our knowledge, one of the best performing non-MOF-containing materials are the  $\text{Ni}_n\text{--CdSe}/\text{CdS}$  core/shell quantum dots, which could produce  $153000 \mu\text{mol g}^{-1} \text{h}^{-1}$  hydrogen under visible light,<sup>[38b,39]</sup> one of the best  $\text{TiO}_2$ -containing materials is the carbon/ $\text{TiO}_2$ /carbon nanotube composite, which had a hydrogen evolution efficiency of  $37600 \mu\text{mol g}^{-1} \text{h}^{-1}$  under the light of an AM 1.5 G solar simulator.<sup>[38b,40]</sup> Although the photocatalytic water-splitting properties of AITCS-1 are far inferior to these materials, it is the first report on the photocatalytic water splitting of crystals of an Al-MOF.

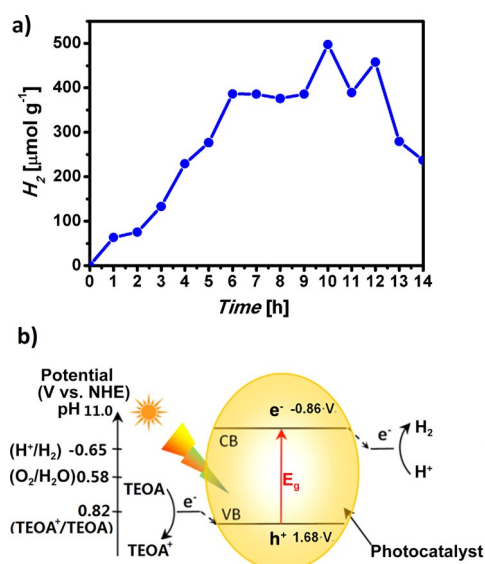


**Figure 11.** a) Photocatalytic amounts of  $\text{H}_2$  evolution for AITCS-1 (synthesized by using a typical procedure for AITCS-1) as a function of light-irradiation time. b) Proposed mechanism of the photocatalytic water-splitting process of AITCS-1 in a solution of  $\text{H}_2\text{O}$  and TEOA (4:1 v/v, 100 mL, pH 11.0).

## Conclusion

We demonstrated how to grow high-quality, large, single-crystal aluminum carboxylate MOFs, resulting in two novel Al-MOFs: AITCS-1 and -2. Based on our experiences, we proposed an efficient method of preparing large, good-quality, single-crystal Al-MOFs. The method includes the incorporation of three techniques: 1) addition of a simple inorganic or organic acid (e.g., HF or formic acid); 2) application of an efficient experimental method, namely, the orthogonal array design ap-

proach; and 3) the use of PXRD to check the crystallinity and identity of the product during investigations. Good-quality, open-framework Al-MOF single crystals should have a PXRD pattern with a peak at a  $2\theta < 10^\circ$ , high crystallinity, and sharp peaks. In addition, we found that changing the solvent polarity and faster cooling rates were favorable to synthesize good-quality, large, single crystals. This method is possibly also useful to synthesize other MOF single crystals. In addition, AITCS-1 and -2 are the first examples of Al-MOFs synthesized based on a tetrahedral-shaped ligand. AITCS-2 is also the first Al-MOF that contains a spiral chain SBU. AITCS-1 and -2 are stable over a wide pH range (1–11), and AITCS-1 is even stable in aqua regia solution. We also found that  $\text{Al}^{3+}$ , not electron-rich ions, could transform a UV-light-absorbing ligand (i.e.,  $\text{H}_4\text{TCS}$ ) into a visible-light absorber; this has not been recognized before.

## Experimental Section

### Synthesis of the MIL-53(Al) single crystal

In a typical synthesis,  $\text{H}_2\text{BDC}$  (0.3456 g, 2.080 mmol),  $\text{Al}(\text{NO}_3)_3 \cdot 9\text{H}_2\text{O}$  (1.56 g, 4.160 mmol), hydrofluoric acid (403  $\mu\text{L}$ , 9.11 mmol, 40% aq), and  $\text{H}_2\text{O}$  (6.0 mL, 330 mmol) were stirred for 10 min in a 14 mL glass vial (diameter: 2.0 cm, height: 5.6 cm). The overall molar ratio of  $\text{Al}(\text{NO}_3)_3/\text{H}_2\text{BDC}/\text{HF}/\text{H}_2\text{O}$  was 2.0:1:4.4:160. The glass vial was then sealed in an autoclave equipped with a Teflon liner (25 mL) and put into an oven. The oven was heated to  $220^\circ\text{C}$  over 1 h, kept at this temperature for 3 d, and then the oven was turned off. The autoclave was cooled to room temperature naturally in the oven; this resulted in colorless, block crystals (Figure 1c) and white powders. Single-crystal XRD analysis was carried out on one of the block crystals, the simulated PXRD pattern of which is given in Figure S4b in the Supporting Information. The product was dried in an oven for 12 h at  $70\text{--}90^\circ\text{C}$ , the PXRD pattern ( $25^\circ\text{C}$ ) of which is shown in Figure S4g in the Supporting Information. In a separate preparation, the crystals were separated from the white powders by utilizing their density differences, and dried in an oven at  $70\text{--}90^\circ\text{C}$  for 12 h; the resulting PXRD pattern is shown in Figure S4h in the Supporting Information.

### Synthesis of AITCS-1

In a typical synthesis with an aqueous solution of HF,  $\text{H}_4\text{TCS}$  (0.040 g, 0.078 mmol),  $\text{Al}(\text{NO}_3)_3 \cdot 9\text{H}_2\text{O}$  (468  $\mu\text{L}$ , 1.0 M aqueous solution of  $\text{Al}(\text{NO}_3)_3 \cdot 9\text{H}_2\text{O}$ , 0.468 mmol), hydrofluoric acid (80  $\mu\text{L}$ , 10% aqueous solution, 4.1 mmol), and  $\text{H}_2\text{O}$  (8.0 mL, 444 mmol) were stirred for 10 min in a 14 mL glass vial. The overall molar ratio of  $\text{Al}(\text{NO}_3)_3/\text{H}_4\text{TCS}/\text{HF}/\text{H}_2\text{O}$  was 6.0:1:5.3:5700. The glass vial was then sealed in an autoclave equipped with a Teflon liner (25 mL) and put into an oven. The temperature of the oven was raised from room temperature to  $220^\circ\text{C}$  with a  $1.0^\circ\text{C min}^{-1}$  heating ramp, kept at  $220^\circ\text{C}$  for 3 d, and then cooled to  $120^\circ\text{C}$  at a rate of  $1.0^\circ\text{C h}^{-1}$ , and to  $25^\circ\text{C}$  with a rate of  $10^\circ\text{C h}^{-1}$ . The resulting colorless block crystals were collected by filtration, washed with DMF and then with  $\text{H}_2\text{O}$ , and dried in a  $90^\circ\text{C}$  oven for 12 h. The overall yield was 39 mg (78 wt%) based on  $\text{H}_4\text{TCS}$ . The purity was checked by PXRD (Figure 7). The product appears light yellow when grounded into powders. IR (KBr):  $\tilde{\nu} = 3685$  (w) ( $\nu(\text{O-H})$  of COOH), 3425 (w), 3020 (w), 2659 (w), 2536 (w), 1948 (w), 1704 (s) ( $\nu(\text{C=O})$  of COOH), 1625 (s) ( $\nu_{\text{asym}}(\text{COO}^-)$ ), 1589 (s), 1540 (s), 1503 (s), 1439 (vs.), 1385 (s) ( $\nu_{\text{sym}}(\text{COO}^-)$ ), 1135 (w), 1318 (w), 1286 (m) ( $\nu(\text{C-O})$  of COOH), 1255

(w), 1192 (w), 1099 (s), 1022 (w), 995 (m), 971 (m), 904 (w), 856 (w), 781 (s), 733 (s), 709 (s), 633 (m), 611 (m), 564 (w), 505 (s), 474 (w), 452 (w),  $413\text{ cm}^{-1}$  (w); elemental analysis calcd (%) for  $[\text{Al}_2(\text{OH})_3(\text{HTCS})_2] \cdot (\text{DMF})_{0.25}(\text{H}_2\text{O})$ : C 57.41, H 3.46, N, 0.29; found: C 57.48, H 3.42, N 0.29. In the syntheses of AITCS-1 with HCOOH reagent (Table S8 in the Supporting Information), the heating procedure was the same as that of the syntheses of MIL-53(Al) single crystals. The amounts of  $\text{H}_4\text{TCS}$  and  $\text{H}_2\text{O}$  were 10 mg (0.020 mmol) and 6.0 mL (333 mmol), respectively.

### Synthesis of AITCS-2

In an optimized preparation for the best-quality single crystals of AITCS-2,  $\text{H}_4\text{TCS}$  (0.020 g, 0.039 mmol),  $\text{Al}(\text{NO}_3)_3 \cdot 9\text{H}_2\text{O}$  (227  $\mu\text{L}$ , 1.0 M aqueous solution of  $\text{Al}(\text{NO}_3)_3 \cdot 9\text{H}_2\text{O}$ , 0.227 mmol), formic acid (0.40 mL, 10.6 mmol), DMF (1.4 mL, 18.2 mmol), and  $\text{H}_2\text{O}$  (0.6 mL, 33.3 mmol) were stirred for 10 min in a 14 mL glass vial. The overall molar ratio of  $\text{Al}(\text{NO}_3)_3/\text{H}_4\text{TCS}/\text{HCOOH}/\text{DMF}/\text{H}_2\text{O}$  was 6.0:1:270:470:850. The glass vial was then sealed in an autoclave equipped with a Teflon liner (25 mL) and put into an oven. The temperature of the oven was raised to  $120^\circ\text{C}$  naturally, kept at  $120^\circ\text{C}$  for 3 d, and then cooled to  $25^\circ\text{C}$  naturally, resulting in colorless, block-like crystals. The crystals were collected by filtration, washed with DMF and then with  $\text{H}_2\text{O}$ , and dried in a  $90^\circ\text{C}$  oven for 12 h. The overall yield was 16.2 mg (63 wt%) based on  $\text{H}_4\text{TCS}$ . The PXRD pattern was obtained (Figure 2, no. 14). IR (KBr):  $\tilde{\nu} = 3451$  (w, br) ( $\nu(\text{O-H})$  of absorbed  $\text{H}_2\text{O}$ ), 1707 (w), 1620 (s) ( $\nu_{\text{asym}}(\text{COO}^-)$ ), 1595 (s), 1546 (s), 1506 (s), 1443 (s), 1390 (w) ( $\nu_{\text{sym}}(\text{COO}^-)$ ), 1315 (w), 1259 (w), 1191 (w), 1105 (s), 1021 (m), 976 (w), 957 (w), 857 (s), 777 (s), 741 (s), 729 (s), 710 (m), 631 (m), 610 (m), 556 (m), 507 (m),  $460\text{ cm}^{-1}$  (w); elemental analysis calcd (%) for  $[\text{Al}_2\text{O}(\text{OH})_3(\text{TCS})_2(\text{H}_2\text{O})_2] \cdot (\text{H}_2\text{O})_6$  (sample was washed thoroughly with  $\text{H}_2\text{O}$  and dried at  $120^\circ\text{C}$  for 12 h before measurements): C 48.77, H 3.73, N 0.0; found: C 48.56, H 3.35, N 0.00.

### X-ray crystallography

Suitable single crystals were selected for single-crystal XRD. The data were collected at 296(2) (AITCS-1), 291(2) (MIL-53), and 150(2) K (AITCS-2) on a Bruker Smart charge-coupled device (CCD) diffractometer with graphite-monochromatic  $\text{MoK}_\alpha$  radiation ( $\lambda = 0.71073\text{ \AA}$ ) from an enhanced optical X-ray tube. Raw data for the structure were obtained by using SAINT, and absorption corrections were applied by using SADABS programs. The structures of AITCS-1 and MIL-53 were solved by direct methods and refined by full-matrix least-squares on  $F^2$  by using the SHELXS-2014 and SHELXL-2014 programs. The structure of AITCS-2 was solved by an intrinsic phasing method and refined by full-matrix least-squares on  $F^2$  by using the SHELXT-2014 and SHELXL-2016 programs. A summary of the crystallographic data, data collection, and refinement parameters for MIL-53 and AITCS-1 and AITCS-2 are provided in Tables S3 and S4 in the Supporting Information. Selected bond lengths and angles for AITCS-1 and -2 are given in Tables S5 and S6 in the Supporting Information.

CCDC 1523998 (AITCS-1), 1523999 (MIL-53(Al single crystal)), and 1551336 (AITCS-2) contain the supplementary crystallographic data for this paper. These data are provided free of charge by The Cambridge Crystallographic Data Centre.

### Acknowledgements

We thank the National Natural Science Foundation of China (NSFC; nos. 21622104, 21371099, 21471080, 21071082, and

21671003), the Key International (Regional) Joint Research Program of the NSFC (no. 21420102002), the Natural Science Foundation of Jiangsu Province (BK20161553), the Natural Science Foundation of Education Department of Jiangsu Province (no. 16KJB150021), the Priority Academic Program Development of Jiangsu Higher Education Institutions, and the Foundation of Jiangsu Collaborative Innovation Center of Biomedical Functional Materials for their funding support.

## Conflict of interest

The authors declare no conflict of interest.

**Keywords:** aluminum · crystal growth · metal–organic frameworks · semiconductors · water splitting

- [1] a) S. Wang, X. Wang, *Small* **2015**, *11*, 3097–3112; b) M. Usman, S. Mendiratta, K.-L. Lu, *Adv. Mater.* **2017**, *29*, 1605071.
- [2] A. Fateeva, P. A. Chater, C. P. Ireland, A. A. Tahir, Y. Z. Khimyak, P. V. Wiper, J. R. Darwent, M. J. Rosseinsky, *Angew. Chem. Int. Ed.* **2012**, *51*, 7440–7444; *Angew. Chem.* **2012**, *124*, 7558–7562.
- [3] M. Gaab, N. Trukhan, S. Maurer, R. Gummaraju, U. Mueller, *Microporous Mesoporous Mater.* **2012**, *157*, 131–136.
- [4] U. Mueller, G. Luinstra, O. M. Yaghi, in *BASF Aktiengesellschaft, Vol. US Pat. 6 617 467* **2004**.
- [5] E. Alvarez, N. Guillou, C. Martineau, B. Bueken, B. Van de Voorde, C. Le Guillouzer, P. Fabry, F. Nouar, F. Taulelle, D. de Vos, J.-S. Chang, K. H. Cho, N. Ramsahye, T. Devic, M. Daturi, G. Maurin, C. Serre, *Angew. Chem. Int. Ed.* **2015**, *54*, 3664–3668; *Angew. Chem.* **2015**, *127*, 3735–3739.
- [6] T. Loiseau, L. Lecroq, C. Volkringer, J. Marrot, G. Ferey, M. Haouas, F. Taulelle, S. Bourrelly, P. L. Llewellyn, M. Latroche, *J. Am. Chem. Soc.* **2006**, *128*, 10223–10230.
- [7] C. G. Wang, J. X. Wu, M. C. Hu, N. Li, N. J. Guan, S. H. Xiang, *J. Porous Mater.* **2012**, *19*, 751–759.
- [8] Y. Han, M. Liu, K. Li, Y. Zuo, Y. Wei, S. Xu, G. Zhang, C. Song, Z. Zhang, X. Guo, *Crystengcomm* **2015**, *17*, 6434–6440.
- [9] Y. Bai, Y. Dou, L.-H. Xie, W. Rutledge, J.-R. Li, H.-C. Zhou, *Chem. Soc. Rev.* **2016**, *45*, 2327–2367.
- [10] B. Seoane, S. Sorribas, Á. Mayoral, C. Téllez, J. Coronas, *Microporous Mesoporous Mater.* **2015**, *203*, 17–23.
- [11] O. L. K. Davies, *Design and Analysis of Industrial Experiments*, 2nd ed., Longman Group Limited, London, **1978**.
- [12] J. Luo, G. Zhu, F. Zhang, Q. Li, T. Zhao, X. Zhu, *Rsc Adv.* **2015**, *5*, 6071–6078.
- [13] C.-S. Tsao, M.-S. Yu, T.-Y. Chung, H.-C. Wu, C.-Y. Wang, K.-S. Chang, H.-L. Chent, *J. Am. Chem. Soc.* **2007**, *129*, 15997–16004.
- [14] B. Chen, X. J. Wang, Q. F. Zhang, X. Y. Xi, J. J. Cai, H. Qi, S. Shi, J. Wang, D. Yuan, M. Fang, *J. Mater. Chem.* **2010**, *20*, 3758–3767.
- [15] Z.-W. Wang, M. Chen, C.-S. Liu, X. Wang, H. Zhao, M. Du, *Chem. Eur. J.* **2015**, *21*, 17215–17219.
- [16] A. L. Spek, *Acta Crystallogr. Sect. D* **2009**, *65*, 148–155.
- [17] V. A. Blatov, A. P. Shevchenko, D. M. Proserpio, *Cryst. Growth Des.* **2014**, *14*, 3576–3586.
- [18] C. Chen, D.-W. Park, W.-S. Ahn, *Appl. Surf. Sci.* **2014**, *292*, 63–67.
- [19] a) Z. Zhang, Y. Zhao, Q. Gong, Z. Li, J. Li, *Chem. Commun.* **2013**, *49*, 653–661; b) R. Sabouni, H. Kazemian, S. Rohani, *Environ. Sci. Pollut. Res. Int.* **2014**, *21*, 5427–5449; c) K. Sumida, D. L. Rogow, J. A. Mason, T. M. McDonald, E. D. Bloch, Z. R. Herm, T. H. Bae, J. R. Long, *Chem. Rev.* **2012**, *112*, 724–781.
- [20] J. Kang, S.-H. Wei, Y.-H. Kim, *J. Am. Chem. Soc.* **2010**, *132*, 1510–1511.
- [21] a) J. Sculley, D. Yuan, H.-C. Zhou, *Energ. Environ. Sci.* **2011**, *4*, 2721–2735; b) M. P. Suh, H. J. Park, T. K. Prasad, D. W. Lim, *Chem. Rev.* **2012**, *112*, 782–835.
- [22] T. A. Makal, J.-R. Li, W. Lu, H.-C. Zhou, *Chem. Soc. Rev.* **2012**, *41*, 7761–7779.
- [23] L. Li, S. Tang, C. Wang, X. Lv, M. Jiang, H. Wu, X. Zhao, *Chem. Commun.* **2014**, *50*, 2304–2307.
- [24] J. B. DeCoste, G. W. Peterson, B. J. Schindler, K. L. Killops, M. A. Browe, J. J. Mahle, *J. Mater. Chem. A* **2013**, *1*, 11922–11932.
- [25] a) A. Yella, C.-L. Mai, S. M. Zakeeruddin, S.-N. Chang, C.-H. Hsieh, C.-Y. Yeh, M. Graetzel, *Angew. Chem. Int. Ed.* **2014**, *53*, 2973–2977; *Angew. Chem.* **2014**, *126*, 3017–3021; b) J. N. Clifford, E. Martinez-Ferrero, A. Viterisi, E. Palomares, *Chem. Soc. Rev.* **2011**, *40*, 1635–1646; c) F. Bureš, *RSC Adv.* **2014**, *4*, 58826–58851.
- [26] a) M. A. Butler, *J. Appl. Phys.* **1977**, *48*, 1914–1920; b) G. Q. Zhang, W. Wang, Q. X. Yu, X. G. Li, *Chem. Mater.* **2009**, *21*, 969–974; c) Z. Sha, J. Wu, *RSC Adv.* **2015**, *5*, 39592–39600; d) A. E. Morales, E. S. Mora, U. Pal, *Revista Mexicana De Física S* **2007**, *53*, 18–22.
- [27] a) G.-L. Wang, J.-X. Shu, Y.-M. Dong, X.-M. Wu, W.-W. Zhao, J.-J. Xu, H.-Y. Chen, *Anal. Chem.* **2015**, *87*, 2892–2900; b) T.-F. Yeh, S.-J. Chen, C.-S. Yeh, H. Teng, *J. Phys. Chem. C* **2013**, *117*, 6516–6524; c) Z. Fang, A. A. Eshbaugh, K. S. Schanze, *J. Am. Chem. Soc.* **2011**, *133*, 3063–3069.
- [28] a) X. Yang, Y. Zhang, F. Li, T. Guo, Y. Wu, F. Jin, M. Fang, Y. Lan, Y. Li, Y. Zhou, Z. Zou, *Dalton Trans.* **2017**, *46*, 8204–8218; b) T. Guo, X. Yang, R. Li, X. Liu, Y. Gao, Z. Dai, M. Fang, H.-K. Liu, Y. Wu, *J. Solid State Chem.* **2017**, *253*, 129–138.
- [29] a) H. Yang, L. Wang, D. Hu, J. Lin, L. Luo, H. Wang, T. Wu, *Chem. Commun.* **2016**, *52*, 4140–4143; b) T. Wu, Q. Zhang, Y. Hou, L. Wang, C. Mao, S.-T. Zheng, X. Bu, P. Feng, *J. Am. Chem. Soc.* **2013**, *135*, 10250–10253.
- [30] W. White, C. D. Sanborn, R. S. Reiter, D. M. Fabian, S. Ardo, *J. Am. Chem. Soc.* **2017**, *139*, 11726–11733.
- [31] J. Gao, J. Miao, Y. Li, R. Ganguly, Y. Zhao, O. Lev, B. Liu, Q. Zhang, *Dalton Trans.* **2015**, *44*, 14354–14358.
- [32] a) W. Wang, J. Fang, S. Shao, M. Lai, C. Lu, *Appl. Catal. B* **2017**, *217*, 57–64; b) J. Liu, R. Li, Y. Hu, T. Li, Z. Jia, Y. Wang, Y. Wang, X. Zhang, C. Fan, *Appl. Catal. B* **2017**, *202*, 64–71; c) Y. Fan, Y. Cui, G.-D. Zou, R.-H. Duan, X. Zhang, Y.-X. Dong, H.-T. Lv, J.-T. Cao, Q.-S. Jing, *Dalton Trans.* **2017**, *46*, 8057–8064.
- [33] Y. An, H. Li, Y. Liu, B. Huang, Q. Sun, Y. Dai, X. Qin, X. Zhang, *J. Solid State Chem.* **2016**, *233*, 194–198.
- [34] W. G. Tu, Y. Zhou, Z. G. Zou, *Adv. Mater.* **2014**, *26*, 4607–4626.
- [35] P. Chowdhury, H. Goma, A. K. Ray, *Chemosphere* **2015**, *121*, 54–61.
- [36] J. He, J. Wang, Y. Chen, J. Zhang, D. Duan, Y. Wang, Z. Yan, *Chem. Commun.* **2014**, *50*, 7063–7066.
- [37] a) T. Zhou, Y. Du, A. Borgna, J. Hong, Y. Wang, J. Han, W. Zhang, R. Xu, *Energ. Environ. Sci.* **2013**, *6*, 3229–3234; b) W. Wang, X. Xu, W. Zhou, Z. Shao, *Adv. Sci.* **2017**, *4*, 1600371.
- [38] a) L. Liao, Q. Zhang, Z. Su, Z. Zhao, Y. Wang, Y. Li, X. Lu, D. Wei, G. Feng, Q. Yu, X. Cai, J. Zhao, Z. Ren, H. Fang, F. Robles-Hernandez, S. Baldelli, J. Bao, *Nat. Nanotechnol.* **2014**, *9*, 69–73; b) X. Li, J. Yu, J. Low, Y. Fang, J. Xiao, X. Chen, *J. Mater. Chem. A* **2015**, *3*, 2485–2534.
- [39] Z.-J. Li, J.-J. Wang, X.-B. Li, X.-B. Fan, Q.-Y. Meng, K. Feng, B. Chen, C.-H. Tung, L.-Z. Wu, *Adv. Mater.* **2013**, *25*, 6613–6618.
- [40] C. Zhao, H. Luo, F. Chen, P. Zhang, L. Yi, K. You, *Energ. Environ. Sci.* **2014**, *7*, 1700–1707.
- [41] We measured atom to atom distances and then deducted the related covalent radii or van der Waals radii (in parentheses) of the related atoms.

Manuscript received: August 7, 2017

Accepted manuscript online: August 28, 2017

Version of record online: October 6, 2017